Journal of Materials Chemistry A

ROYAL SOCIETY OF CHEMISTRY

PAPER

View Article Online
View Journal

Cite this: DOI: 10.1039/d6ta01036a

$Na_3LaP_2O_8$-enabled microstructural engineering for enhanced mechanical robustness and ionic transport behavior in NaSICON solid electrolytes

Xingyu Liu, *[a] Jürgen Peter Gross, [a] Qianli Ma, [b] Frank Tietz, [bc] Jürgen Malzbender [a] and Ruth Schwaiger[a]

Received 3rd February 2026
Accepted 27th March 2026

DOI: 10.1039/d6ta01036a

rsc.li/materials-a

NaSICON-type $Na_{1+x}Zr_2Si_xP_{3-x}O_{12}$ ($0 \leq x \leq 3$, NZSP) were synthesized *via* a solution-assisted solid-state reaction method, and the effect of $Na_3LaP_2O_8$ (NLP) addition on their microstructure, mechanical properties, and electrical performance was systematically investigated. NLP incorporation refined the grain structure, yielding a more uniform grain size distribution, reduced porosity, and suppressed microcrack formation, which collectively enhanced densification and mechanical performance. The optimized composition (2.5 mol% NLP) exhibited substantial increases in elastic modulus, hardness and fracture toughness compared to original NZSP. However, excessive NLP addition hindered ionic transport due to the insulating nature of NLP, revealing a trade-off between mechanical robustness and ionic conductivity. This work establishes a quantitative correlation between the mechanical and electrical properties of NLP-modified NZSP and provides a design strategy for mechanically reinforced, high-performance solid-electrolytes for all-solid-state sodium batteries.

1. Introduction

Secondary batteries, serving as a pivotal technology for clean energy, enable efficient storage and release of electrical energy. Their widespread application across various sectors plays a vital role in advancing carbon neutrality objectives. Although lithium-ion batteries (LIBs) dominate the markets of portable electronics and electric vehicles due to their high energy density and low self-discharge rate, the limited availability and escalating costs of lithium constrain their further development. In contrast, sodium-ion batteries (SIBs), possessing electrochemical properties similar to LIBs along with advantages such as resource abundance and stable cost development, have emerged as a promising alternative.[1]

Conventional liquid electrolytes suffer from challenges such as high flammability, poor thermal stability, and undesirable side reactions. In response, all-solid-state batteries (ASSBs), which employ solid-electrolytes (SEs), have attracted significant interest due to their ability to mitigate these issues while their excellent mechanical properties, effectively suppressing detrimental Li-dendrite growth, making them strong candidates for next-generation clean energy storage.[2,3] Among various SEs, NaSICON (sodium superionic conductor)-type inorganic oxide ceramics stand out as leading candidates for use in solid-state SIBs, owing to their exceptional chemical and electrochemical stability. NaSICON-structured $Na_{1+x}Zr_2Si_xP_{3-x}O_{12}$ ($0 \leq x \leq 3$, NZSP) SEs exhibit remarkable ionic conductivity (10^{-4} to 10^{-3} S cm^{-1} at room temperature (RT)[4,5]) and demonstrate good electrochemical compatibility with sodium metal anodes.[6] For instance, Ma *et al.* synthesized $Na_{3.4}Zr_2Si_{2.4}P_{0.6}O_{12}$ *via* a solution-assisted solid-state reaction, achieving a high total ionic conductivity of 5×10^{-3} S cm^{-1} at 25 °C and furthermore demonstrated good cycling performance in symmetric battery cells at RT.[7]

Current research on SEs primarily emphasizes electrochemical properties, including ionic conductivity,[8] cycling stability,[9] and interfacial ion transport.[10] However, the number of investigations of their mechanical properties is still limited, despite their critical importance for practical applications. Dendritic formation and growth in metal-based batteries, a prevalent issue, lead to internal short circuits and hence failure of the cell.[1,11] Studies have demonstrated that the mechanical properties of SEs are crucial in suppressing dendrite propagation.[12,13] High fracture toughness avoids crack propagation,[14,15] thereby enhancing battery stability and cycle life.[16] Additionally, appropriate flexibility and mechanical strength facilitate electrolyte processing into thin films, reducing internal resistance and improving energy density.[17] Despite its significance, characterization of the mechanical properties of NaSICON-type SEs is available only for specific

[a]Forschungszentrum Jülich GmbH, Institute of Energy Materials and Devices, Structure and Function of Materials (IMD-1), 52425 Jülich, Germany. E-mail: xing.liu@fz-juelich.de

[b]Forschungszentrum Jülich GmbH, Institute of Energy Materials and Devices, Materials Synthesis and Processing (IMD-2), 52425 Jülich, Germany

[c]Forschungszentrum Jülich GmbH, Institute of Energy Materials and Devices, Helmholtz Institute Münster-Ionics in Energy Storage (IMD-4), 52425 Jülich, Germany

compositions. Nonemacher *et al.* systematically characterized the fracture toughness, hardness and modulus of NZSP and Al/Y-substituted NZSP.[18] Gross *et al.* highlighted that insufficient sodium content leads to increased bloating, glassy phase formation, and the development of secondary phases, the latter of which can induce microcracks within the NaSICON material.[19] Hitesh *et al.* investigated the mechanical behavior of NZSP sintered and annealed at different temperatures using spark plasma sintering, revealing that samples annealed at 1100 °C for 20 hours exhibited improved hardness (from 5.4 to 6.7 GPa) and fracture toughness (from ~2.3 to 2.6 MPa $m^{0.5}$).[20]

The ionic conductivity of polycrystalline ceramics is governed by both bulk and grain boundary contributions, with overall conductivity predominantly dictated by grain boundary resistance. Theoretical calculations indicate that the energy required to mechanically separate grain boundaries can be significantly lower than that of the bulk material,[21] emphasizing the importance to improve the mechanical strength of grain boundaries. Thus, optimizing grain boundary properties appears also to be one of the keys to enhance total ionic conductivity. Zhang *et al.* demonstrated that introducing La^{3+} into NZSP generates self-formed La-containing phosphate phases that enhance densification and markedly improve both bulk and grain-boundary ionic conductivities, while ionic–liquid interfacial engineering further boosts full-cell performance.[22] More recently, direct addition of NLP into NZSP was shown to reduce grain-boundary resistance and achieve a high ionic conductivity of 7.1×10^{-3} S cm^{-1} at 25 °C, together with improved electrochemical stability and dendrite tolerance.[23] Although these studies clearly confirm the electrochemical advantages of NLP and report the associated microstructural changes, they do not include mechanical characterization; consequently, the mechanical implications of NLP incorporation—and their relevance to grain-boundary-related ionic transport—remain unaddressed.

Building on this context, the present work systematically investigates the influence of NLP content on the mechanical properties of $Na_{3.4}Zr_2Si_{2.4}P_{0.6}O_{12}$ (elastic modulus, hardness, and fracture toughness), with fracture toughness quantified *via* micro-pillar splitting and benchmarked against Vickers indentation. Microstructural analysis identifies NLP-induced strengthening effects, including grain refinement and reduced microcracking, and establishes how these features correlate with ionic conduction behavior. This study provides the first experimental assessment of the mechanical properties associated with NLP incorporation in NZSP and clarifies how mechanical stability interacts with grain-boundary ionic transport, offering guidance for the design and optimization of NaSICON-type solid electrolytes.

2. Experimental details

2.1 Materials

The compositions and sintering parameters of the investigated materials are listed in Table 1. All samples were synthesized in the same batch under identical processing conditions. NZSP and NZSP with NLP powders were prepared by the solution-assisted solid-state reaction method. This method enables better control of particle morphology and grain size, facilitating an optimized sintered microstructure for NaSICON-type materials.[7,24] $La(NO_3)_3 \cdot 6H_2O$ (Sigma-Aldrich, 99%), $NaNO_3$ (VWR International, 99%), $NH_4H_2PO_4$ (Merck KGaA, 99%), $Si(OCH_2CH_3)_4$ (Merck KGaA, 99%), and $ZrO(NO_3)_2$ (Sigma-Aldrich, 99%) were used as starting materials. All the chemicals used in this work were of analytical grade. Stoichiometric amounts of $NaNO_3$ and $ZrO(NO_3)_2$ were first dissolved in deionized water to form a clear solution. Under continuous stirring, tetraethyl orthosilicate $[Si(OCH_2CH_3)_4]$ was gradually introduced. After the hydrolysis of the silicon precursor, the calculated quantity of $NH_4H_2PO_4$ was subsequently added while maintaining agitation. The resulting uniform aqueous mixture rapidly evolved into zirconium oxyphosphate complexes. The obtained precursor solution was then dried at 85 °C to yield a solid powder. This powder was subsequently calcined at 800 °C for 3 h to obtain a white powder. Following calcination, the material underwent ball milling in 96% ethanol using zirconia balls for a period of 48 h. After the milling process, the powder was dried at 70 °C for 12 h, yielding the NZSP precursor powder. The synthesis of NLP-modified NZSP followed an identical procedure, except that additional stoichiometric amounts of $NaNO_3$, $La(NO_3)_3 \cdot 6H_2O$, and $NH_4H_2PO_4$ were introduced into the initial NZSP precursor solution. The resulting powders were subsequently subjected to an additional ball-milling step in absolute ethanol to ensure compositional homogeneity.

The powders were loaded into a cylindrical model with a diameter of 13 mm and compacted by uniaxial pressing at RT under a pressure of 113 MPa. After sintering, pellets with a thickness of about 1 mm were obtained. The mechanical properties were evaluated by multiple measurements taken at different locations on a single representative pellet, a standard approach that averages out local variations. Electrochemical impedance was measured on three separately sintered pellets to capture batch-to-batch differences and ensure reproducible ionic conductivity.

2.2 Impedance spectroscopy

For conductivity measurements, gold electrodes were deposited onto pellets by a sputter coater (Ted Pella Inc., Cressington 108

Table 1 The compositions and sintering parameters of the investigated materials

Material	Label	Sintering temperature	Duration
$Na_{3.4}Zr_2Si_{2.4}P_{0.6}O_{12}$	Original NZSP	1260 °C	5 h
$Na_{3.4}Zr_2Si_{2.4}P_{0.6}O_{12}$ + 1 mol% $Na_3LaP_2O_8$	NZSP-1NLP	1260 °C	5 h
$Na_{3.4}Zr_2Si_{2.4}P_{0.6}O_{12}$ + 2.5 mol% $Na_3LaP_2O_8$	NZSP-2.5NLP	1260 °C	5 h
$Na_{3.4}Zr_2Si_{2.4}P_{0.6}O_{12}$ + 5 mol% $Na_3LaP_2O_8$	NZSP-5NLP	1260 °C	5 h

Auto) for Au|NZSP (-NLP)|Au symmetric cells. Electrochemical impedance spectroscopy measurements were conducted using two commercial analyzers, namely a Keysight E4991B and a Novocontrol Alpha-A. The impedance spectra were collected over frequency ranges of 3 GHz–1 MHz and 3 MHz–1 Hz, respectively, using an alternating current (AC) perturbation amplitude of 20 mV at RT. The acquired impedance data were analyzed and fitted with Z-view software (Scribner Associates Inc.), and the ionic conductivity was determined from the pellet geometry.

2.3 Characterization

Before performing mechanical and microstructural characterization, the cross-section of each respective sample was polished. For this, the sample was embedded in epoxy resin and then ground sequentially using SiC sandpapers with grit sizes ranging from 80 to 2500 and water-free lubricant. The ground cross section was further refined by stepwise polishing using water-free diamond suspensions with decreasing particle sizes from 3 μm to 0.5 μm. Since NZSP is moisture-sensitive, the use of a water-free grinding and polishing mitigates possible influences of moisture on the mechanical properties of the samples.

X-ray diffraction (XRD) patterns were recorded with an EMPYREAN diffractometer (PANalytical, Kassel, Germany) with Cu-Kα radiation (time per step = 0.5 s, step size = 0.0131°) for the qualitative phase analysis of the samples. Quantitative phase analysis and lattice parameter determination were performed using Rietveld refinement (software: TOPAS v.6, Bruker AXS). The necessary crystal structure files were taken from the Inorganic Crystal Structure Database (ICSD). To enhance the accuracy of the analysis, each sample was ground into a fine powder before conducting the XRD measurements.

Field emission scanning electron microscopy (FE-SEM, MERLIN™, Carl Zeiss Microscopy, Oberkochen, Germany) was employed to capture scanning electron microscopy (SEM) images. The sample surface was deposited by iridium before SEM characterization to enhance surface conductivity with an accelerating current of 10 mA for 25 s. Phase elemental composition was analyzed using energy-dispersive X-ray spectroscopy (EDX) with an X-Max Extreme detector (Oxford Instruments, High Wycombe, UK). Porosities were estimated by analyzing SEM images using the ImageJ software.[25]

Thermal etching was used to reveal the sample's grain size distribution. The polished sample was heated to 1100 °C in a furnace, held for 1 h, and cooled to RT within the furnace. SEM analysis was then performed to characterize the grain size.

2.4 Mechanical methods

The elastic modulus E and hardness H of the samples were determined by micro-indentation. These measurements were performed using a FISCHERSCOPE® HC 100 instrument equipped with a Vickers diamond tip (Helmut Fischer GmbH, Sindelfingen, Germany). An "enhanced stiffness procedure" method based on cyclic indentation was employed for the measurements. For each measurement a number of 8 loading and unloading cycles were performed whereby the maximum load was increased by 50% with each cycle up to a maximum target load of 1000 mN. A representative load–displacement curve is shown in Fig. S1 in the SI. The E and H values were determined in accordance with DIN ISO 14577-1:2015 (ref. 26) using the unloading slope of the load–displacement curves, assuming a Poisson's ratio of 0.27.[19] A minimum of 20 indentations were performed on each specimen, with a lateral spacing of 50 μm between adjacent indents.

The conventional Vickers indentation fracture (VIF) method was employed to evaluate the fracture toughness of the samples using a Vickers hardness tester MV-IS (Buehler Ltd, Lake Bluff, USA). Indentations were performed under three different loads (0.5 N, 1 N, and 2 N) in order to induce cracks. For each load at least 10 indentations were performed. The residual indentation imprints were subsequently captured, and crack lengths were quantified using a laser confocal microscope (LEXT OLS6000, Olympus, Hamburg, Germany). Owing to the ratio between the crack length (l) and half diagonal of the indent (a) falling within the range of $0.25 \leq l/a \leq 2.5$, the Palmqvist crack model was adopted for the evaluation of fracture toughness.[27,28] The K_{IC} was determined according to the following equation:[29]

$$K_{IC} = 0.0515 \frac{P}{C^{3/2}} \quad (1)$$

where, P is the applied load, C is the sum of the crack length and the half diagonal.

Besides the VIF tests, fracture toughness was further evaluated using the micro-pillar splitting technique. Plasma focused ion beam scanning electron microscope (PFIB-SEM, Helios 5, Thermo Fisher Scientific, US) was used to fabricate micro-pillars. Hereby a two-step process was applied, where first rough pillars with a slightly larger diameter were milled with an ion beam accelerating voltage of 30 kV and a beam current of 1 nA, subsequently the pillars where polished to the target diameter and height (5 μm) using a beam current of 0.1 nA. This specific diameter to height aspect ratio of 1 : 1 was selected to minimize the influence of potential residual stresses.[30]

An *in situ* nanoindenter (FT-NMT04, FemtoTools AG, a Swiss-based company acquired by Oxford Instruments, UK) equipped with a Berkovich tip was used for splitting the pillars. Load–displacement data were collected and analyzed to extract the critical load. The fracture toughness was calculated using the following equation:[30]

$$K_{IC} = \gamma \times \frac{P_c}{R^{3/2}} \quad (2)$$

where, P_c represents the critical load for pillar splitting, R denotes the pillar radius, and γ is a dimensionless coefficient that accounts for the material's elastic–plastic properties, crack propagation behavior, and the geometry of the indenter. The coefficient γ can be determined based on the following relationship:[30–32]

$$\gamma = 0.0149 \times \left(\frac{E}{H}\right) + 0.057 \quad (3)$$

To ensure consistency with the critical load used in the micro-pillar splitting method, the E and H were determined at

the corresponding load. A 5 × 5 array of nanoindentations was performed near the micro-pillars by a nano indenter (G200X, KLA Instruments, Milpitas, CA, USA) equipped with a diamond Berkovich tip) to obtain accurate measurements of E and H required for fracture toughness calculations. Continuous Stiffness Measurement (CSM) mode was employed, which applies a small high-frequency oscillatory load superimposed on the primary load to continuously measure changes in hardness and elastic modulus as a function of indentation depth.

3. Results

3.1 Ionic conductivity

Impedance spectra of the original and modified NZSP (where NZSP-1NLP, NZSP-2.5NLP and NZSP-5NLP are collectively referred to as modified NZSP), measured at RT, are shown in Fig. 1. This study combines the frequency ranges of both impedance analyzers. The reason of applying a special high frequency system is the very small time constant (τ) of the bulk response of NZSP-NLP materials corresponding to very high frequencies. At RT, the impedance spectra often display only a single, or in some cases partial, semicircular feature associated with the grain-boundary contribution, which can be attributed to the restricted upper frequency limit (up to several MHz) of conventional impedance spectroscopy equipment with normal frequency range (NF). It is therefore challenging to precisely distinguish between the contributions from bulk and grain-boundary. To make up for this deficiency, a high frequency (HF) impedance spectroscopy system with frequency limit up to 3 GHz was applied. As shown in Fig. 1, two complete semicircles are clearly exhibited, guaranteeing the clarity in distinguishing the bulk (HF semi-circle) from the grain-boundary contribution (NF semi-circle). The results of original NZSP and NZSP-2.5NLP were taken from previously published reports ref. 7 and 23, respectively. Additional electrochemical results are provided in the SI (Fig. S2–S5).

Table 2 summarizes the resistances and ionic conductivities of original and modified NZSP derived from equivalent-circuit fitting. The bulk resistances are similar, whereas the grain-boundary resistance first decreases with NLP addition and then increases at higher contents. This trend suggests that a moderate amount of NLP alleviates grain-boundary blocking and facilitates Na^+ transport. Notably, NZSP-2.5NLP reveals a high total conductivity of 7.1×10^{-3} S cm^{-1}, surpassing that of reported polycrystalline oxide SEs.[4] Zhang *et al.* attempted La substitution for Zr in NZSP, but La did not incorporate into the lattice and an NLP phase formed. The highest σ_{total} achieved was 3.4 mS cm^{-1} at RT, much lower than that of the present work.[22]

Table 2 Resistances and ionic conductivities of the original and modified NZSP at RT

	Original NZSP	NZSP-1NLP	NZSP-2.5NLP	NZSP-5NLP
R_{bulk} (Ω cm)	67	86	78	88
R_{gb} (Ω cm)	125	68	62	112
R_{total} (Ω cm)	192	154	140	200
σ_{bulk} (S cm^{-1})	1.5×10^{-2}	1.2×10^{-2}	1.3×10^{-2}	1.1×10^{-2}
σ_{total} (S cm^{-1})	5.2×10^{-3}	6.4×10^{-3}	7.1×10^{-3}	5.0×10^{-3}

3.2 Phase composition

As shown in Fig. 2, the major crystalline phase in original NZSP and modified NZSP has NaSICON structure. ZrO_2 is observed in all samples, which is a common secondary phase in NaSICON SEs.[33]

Rietveld refinement was employed to determine the crystallographic characteristics, and the fitting results are shown in Fig. S6 and Table 3. In this study, the original NZSP exhibited a monoclinic phase. In the modified samples, severe overlap of Bragg reflections arising from coexisting NaSICON-type phases with similar lattice parameters prevents reliable differentiation between monoclinic and rhombohedral symmetry. As the

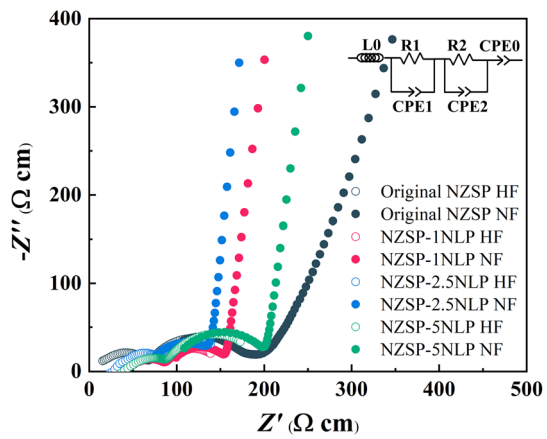

Fig. 1 Impedance spectra of original and modified NZSP with fitted equivalent circuits. The grain-boundary semicircle is smaller in NZSP-2.5NLP, indicating reduced grain-boundary resistance.

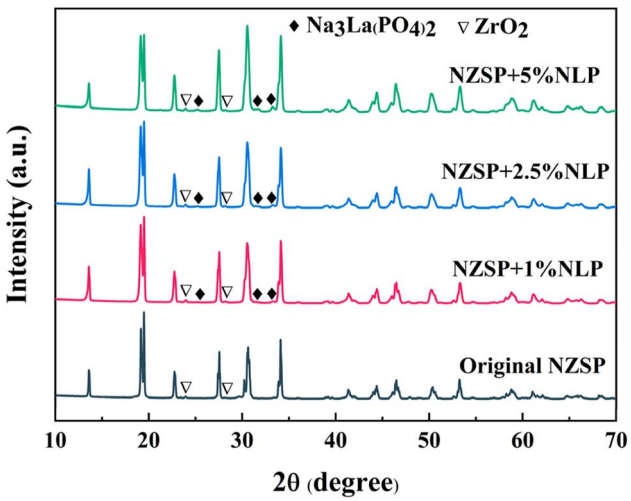

Fig. 2 XRD patterns of original and modified NZSP. All samples exhibit the NaSICON primary phase and the ZrO_2 secondary phase. With NLP addition, it emerged as an additional secondary phase, whose peak intensities increased with its content.

Table 3 Rietveld analysis results. The β angle is applicable only to monoclinic phases and is therefore marked as "not applicable (NA)" for rhombohedral and orthorhombic structures

Sample	Phase	Space group	wt%	a [Å]	b [Å]	c [Å]	β [°]
Original NZSP	$Na_{3.4}Zr_2Si_{2.4}P_{0.6}O_{12}$	$C2/c$	99.7	15.742	9.100	9.193	124.33
	ZrO_2	$P2_1/c$	0.3	5.144	5.210	5.311	99.22
NZSP-1NLP	$Na_{3.4}Zr_2Si_{2.4}P_{0.6}O_{12}$	$R\bar{3}c$	98.7	9.095	9.095	22.928	NA
	ZrO_2	$P2_1/c$	0.6	5.144	5.210	5.311	99.22
	$Na_3La(PO_4)_2$	$Pca2_1$	0.7	14.160	5.360	18.714	NA
NZSP-2.5NLP	$Na_{3.4}Zr_2Si_{2.4}P_{0.6}O_{12}$	$R\bar{3}c$	97.9	9.096	9.096	22.927	NA
	ZrO_2	$P2_1/c$	0.5	5.144	5.210	5.311	99.22
	$Na_3La(PO_4)_2$	$Pca2_1$	1.6	14.160	5.360	18.714	NA
NZSP-5NLP	$Na_{3.4}Zr_2Si_{2.4}P_{0.6}O_{12}$	$R\bar{3}c$	97	9.076	9.076	22.785	NA
	ZrO_2	$P2_1/c$	0.3	5.144	5.210	5.311	99.22
	$Na_3La(PO_4)_2$	$Pca2_1$	2.7	14.160	5.360	18.714	NA

monoclinic model did not significantly improve the refinement quality and introduces additional lattice parameters, the rhombohedral structure was adopted as a simplified and stable refinement model (see detailed discussion under Fig. S6). After elucidating the crystal structure, the lattice parameters were determined, and the phase fractions were quantitatively analyzed. Rietveld refinement indicates the presence of a small amount of monoclinic ZrO_2 (0.3–0.6 wt%) in all samples, without a clear systematic dependence on NLP content.

3.3 Microstructure

In Fig. 3 the polished cross-sections of original NZSP and the modified NZSP are shown as SEM micrographs at low magnification. In all samples voids can be observed in an irregular shape, predominantly located at the junctions between grains. Compared to the original NZSP sample shown in Fig. 3(a), the number and size of voids in the NZSP-2.5NLP and NZSP-5NLP samples, as illustrated in Fig. 3(c and d), are significantly reduced. Porosity analysis conducted using ImageJ software reveals that the porosity values for the original NZSP, NZSP-1NLP, NZSP-2.5NLP, and NZSP-5NLP are 7.1%, 4.2%, 2.5%, and 1.1%, respectively.

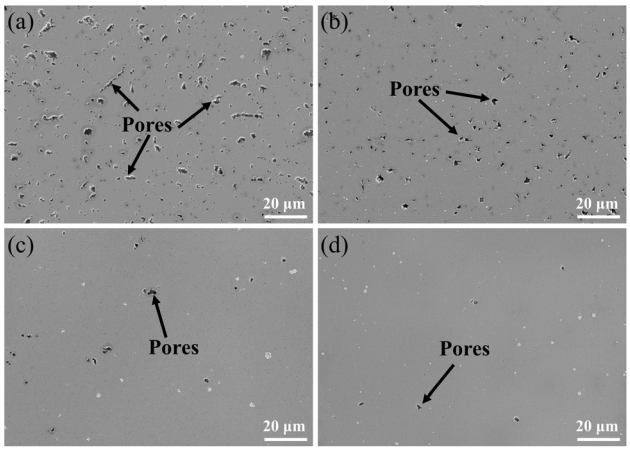

Fig. 3 Porosity of (a) original NZSP; (b) NZSP-1NLP; (c) NZSP-2.5NLP and (d) NZSP-5NLP. With the increase of NLP content, the porosity of NZSP gradually decreases.

In Fig. 4 the polished cross-section of the original and modified NZSP samples are shown as high-magnification SEM micrographs. The corresponding larger-scale images in Fig. S7 reveals the presence of ZrO_2 in each sample. Notably, a significant number of cracks is evident in the original NZSP and NZSP-1NLP; however, as the NLP content increases, these cracks are progressively reduced and eventually eliminated, as shown in Fig. 4(c and d). In the modified NZSP, the NLP occurs as allotriomorphs concentrated along grain boundaries. EDX line-scanning in Fig. S8 reveals a pronounced peak-type La concentration at the interface, forming a continuous and stable enrichment zone.

Thermal etching was used to reveal the grain-boundaries and thus enable the measurements of the grain sizes of original NZSP and modified NZSP (see corresponding SEM micrographs and grain size distributions obtained by Image analysis in Fig. 5). The original NZSP shows a wide grain size distribution, with large grains (~3–6 μm) and small grains (<1.5 μm) randomly distributed. A similar pattern is observed in NZSP-1NLP. In contrast, NZSP-2.5NLP and NZSP-5NLP exhibit a more uniform grain distribution, with the majority of grains concentrated in the 1–3 μm range.

3.4 Mechanical characterization

3.4.1 Elastic modulus *E* and hardness *H*. The results of elastic modulus and hardness are presented in Fig. 6 and Table 4. The original NZSP exhibits the lowest elastic modulus 69.4 ± 7.2 GPa, while NZSP-2.5NLP and NZSP-5NLP show significantly higher values of 79.9 ± 4.3 GPa and 80.2 ± 1.2 GPa, respectively. Notably, the elastic modulus of NZSP-5NLP remains stable with increasing displacement depth, whereas other electrolyte materials exhibit a decreasing trend. This phenomenon may be attributed to porosity. In general, as the applied load (displacement) increases, the effective deformation area of the indentation expands. Pores in this area are prone to deformation or collapse under load, leading to a reduction in the elastic modulus with increasing displacement depth. In contrast, the exceptionally low porosity of NZSP-5NLP minimizes this effect, allowing its elastic modulus to remain nearly unchanged. In addition, the hardness values measured at 400 mN and 1000 mN agree within experimental uncertainty for all samples,

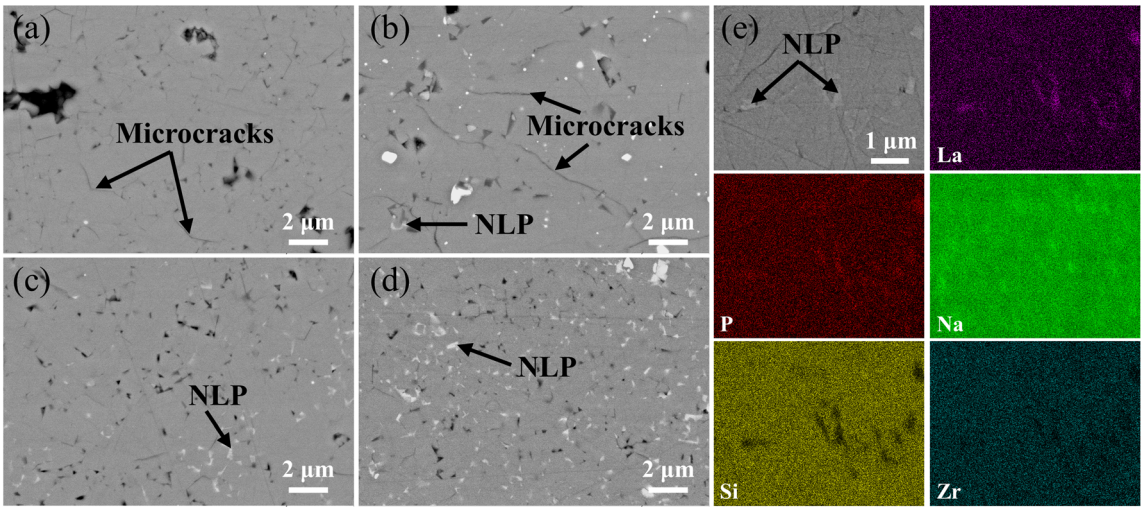

Fig. 4 Backscattered electron SEM images of (a) original NZSP; (b) NZSP-1NLP; (c) NZSP-2.5NLP; (d) NZSP-5NLP and (e) EDS mapping of secondary phase. Significantly reduced microcracks can be found in NZSP-2.5NLP and NZSP-5NLP. The secondary phase is enriched in La, P, and Na at the interface, while Si and Zr show weak signals, confirming-together with XRD-that this phase is the NLP.

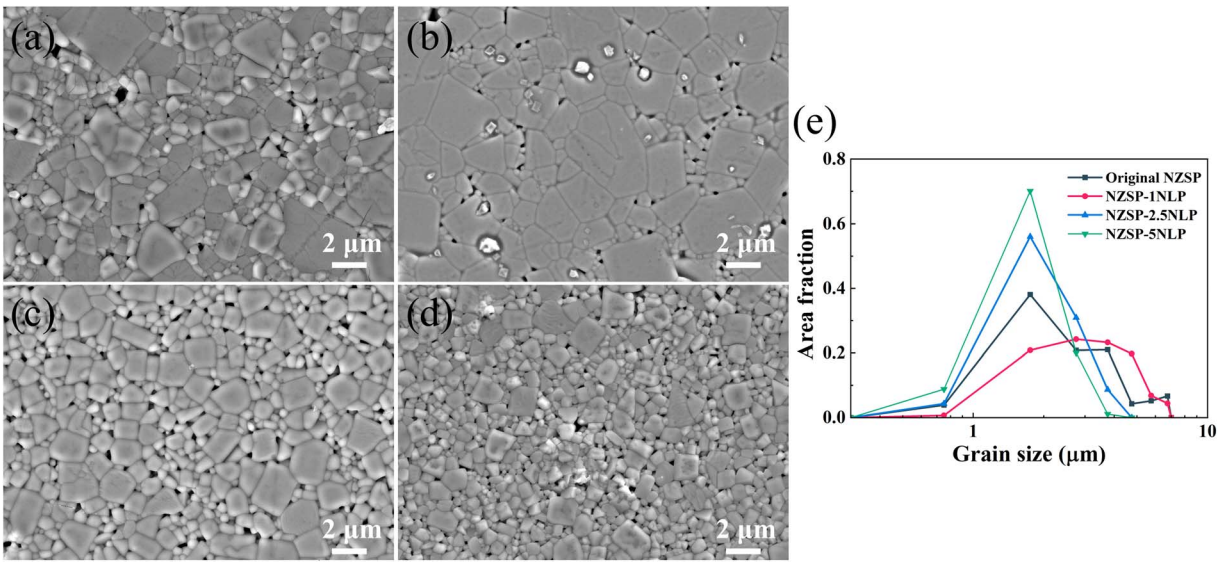

Fig. 5 SEM images after thermal etching: (a) original NZSP; (b) NZSP-1NLP; (c) NZSP-2.5NLP, (d) NZSP-5NLP and (e) grain size distributions. With the increase of NLP content, the grain size decreases and the distribution becomes more uniform.

suggesting that indentation size effects are not significant within the investigated load range.

3.4.2 Fracture toughness

3.4.2.1 VIF method. Fracture toughness is a key metric for evaluating the resistance of solid electrolyte to crack propagation, crucial for assessing the mechanical stability of solid-state batteries. As illustrated in Fig. 7, the fracture toughness values determined using the VIF approach under loads of 0.5, 1, and 2 N remain within the same range of 0.6–0.9 MPa $m^{0.5}$. The differences among the loads fall within the experimental scatter indicated by the error bars, and no statistically significant dependence of the fracture toughness on load is observed. The original NZSP value at 0.5 N was excluded due to extensive crushing around the indentation, making crack length measurement impossible, as shown in Fig. S9 of the SI.

Typical indentation imprints under the load of 1 N are shown in Fig. 8. The ratio of crack lengths to half-diagonals (l/a) for all samples ranges from 0.9 to 1.8, which complies with the Palmqvist crack system requirement of $0.25 \leq l/a \leq 2.5$. The original NZSP and NZSP-1NLP exhibited multiple fine cracks at the indentation tips, propagating along the grain boundaries, indicating an intergranular fracture mode. In contrast, NZSP-2.5NLP and NZSP-5NLP exhibited distinct cracks with tortuous paths emanating from the indentation tips, suggesting a mixed fracture mode involving both transgranular and intergranular fracture. As shown in the inset of Fig. 8(c), the cracks in NZSP-2.5NLP exhibited slight deflection upon encountering

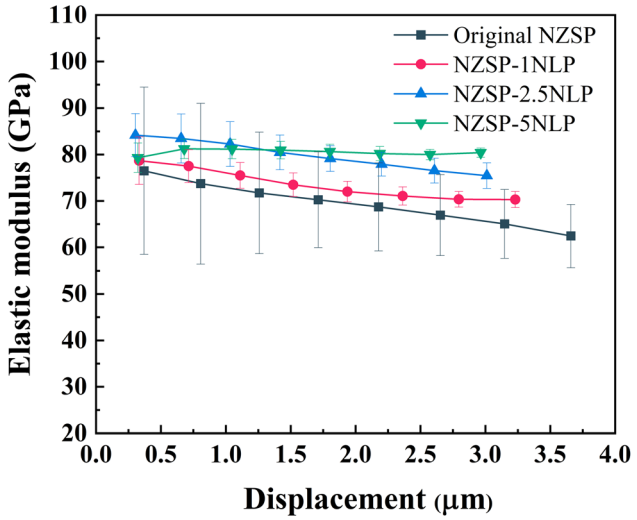

Fig. 6 Elastic modulus of original NZSP and modified NZSP. NZSP-2.5NLP and NZSP-5NLP exhibit higher elastic modulus.

Table 4 The hardness of original NZSP and modified NZSP under different loads

Sample	Hardness (400 mN)/(GPa)	Hardness (1000 mN)/(GPa)
Original NZSP	4.9 ± 1.2	4.6 ± 1.0
NZSP-1NLP	6.7 ± 0.3	6.2 ± 0.3
NZSP-2.5NLP	8.1 ± 1.0	7.5 ± 0.6
NZSP-5NLP	7.9 ± 0.2	7.6 ± 0.2

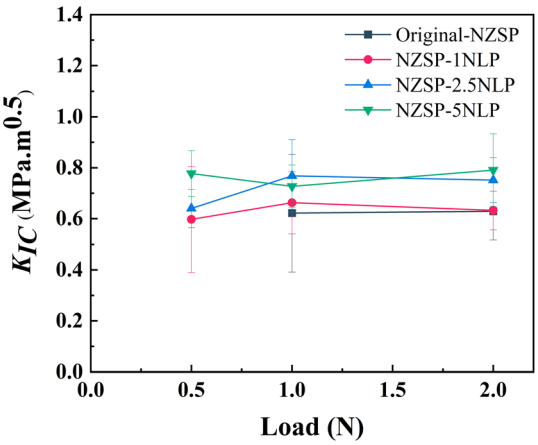

Fig. 7 Fracture toughness of original NZSP and modified NZSP. The fracture toughness of NZSP-2.5NLP and NZSP-5NLP is relatively higher.

ZrO_2 particles, attributed to the high modulus of ZrO_2, which exceeds 200 GPa.[34]

Under a load of 0.5 N, the fracture toughness of NZSP-2.5NLP is slightly lower than those under other load conditions, likely due to measurement errors in crack length. As shown in Fig. S9, the cracks at 0.5 N are short and curved, with a complex nonlinear morphology increasing measurement uncertainty.

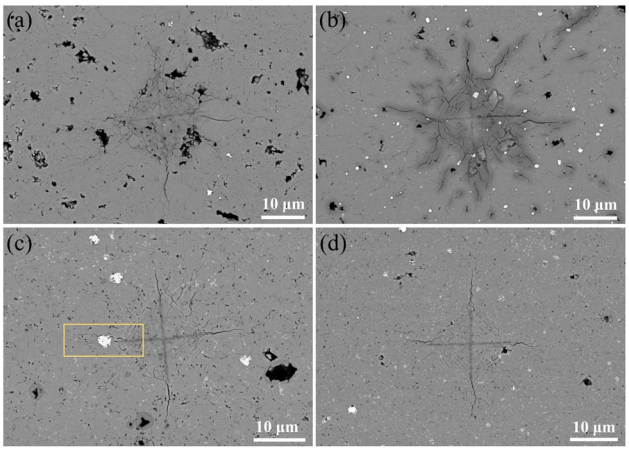

Fig. 8 Backscattered electron SEM imprint images after application a force of 1 N: (a) original NZSP; (b) NZSP-1NLP; (c) NZSP-2.5NLP and (d) NZSP-5NLP. Both transgranular and intergranular fractures occur in NZSP-2.5NLP and NZSP-5NLP.

3.4.2.2 Micro-pillar splitting method. The original NZSP and the ionically superior NZSP-2.5NLP were utilized to investigate fracture toughness by the micro-pillar splitting method for comparison with the results of the VIF method. Fig. 9 displays the FIB-milled micro-pillars, the SEM images after indentation splitting, and the typical load–displacement curves obtained during testing. When selecting the locations for the micro-pillars, areas with high porosity were deliberately avoided to minimize the influence of pores on the pillars. However, as mentioned above, the original NZSP exhibited a higher porosity, and as depicted in Fig. 9(a), the milling positions inevitably included porous regions, albeit ensuring that the surfaces of the micro-pillars were free from obvious pores. According to Fig. 5(e), most grains are ≤5 μm, and the 5 μm micropillars interacted with multiple grains rather than a single grain. Each pillar is estimated to involve several grains (~4–8 in original NZSP and ~6–10 in NZSP-2.5NLP), indicating that crack propagation occurs across multiple grain boundaries and represents an effective polycrystalline response. Therefore, the measured fracture toughness is more likely to reflect intrinsic microstructural differences rather than the number of grains involved.

As can be observed from Fig. 9(c and f), the first peak in the load–displacement curve corresponds to the critical load value, indicating the initial damage in the pillar at this stage. As displacement progresses, the load exhibits a fluctuating upward trend until the sample undergoes ultimate compressive failure. Significantly, during the transition from critical load to structural failure, sudden localized load drops observed in the curve correspond to the initiation and propagation of new cracks. As the pillar splitting technique considers only the load and energy associated with the initiation and propagation of the dominant crack, the development of secondary cracking after reaching the critical load has no effect on the evaluated fracture toughness. The critical load at which cracking occurs in both original NZSP and NZSP-2.5NLP micro-pillars was measured to be below 15

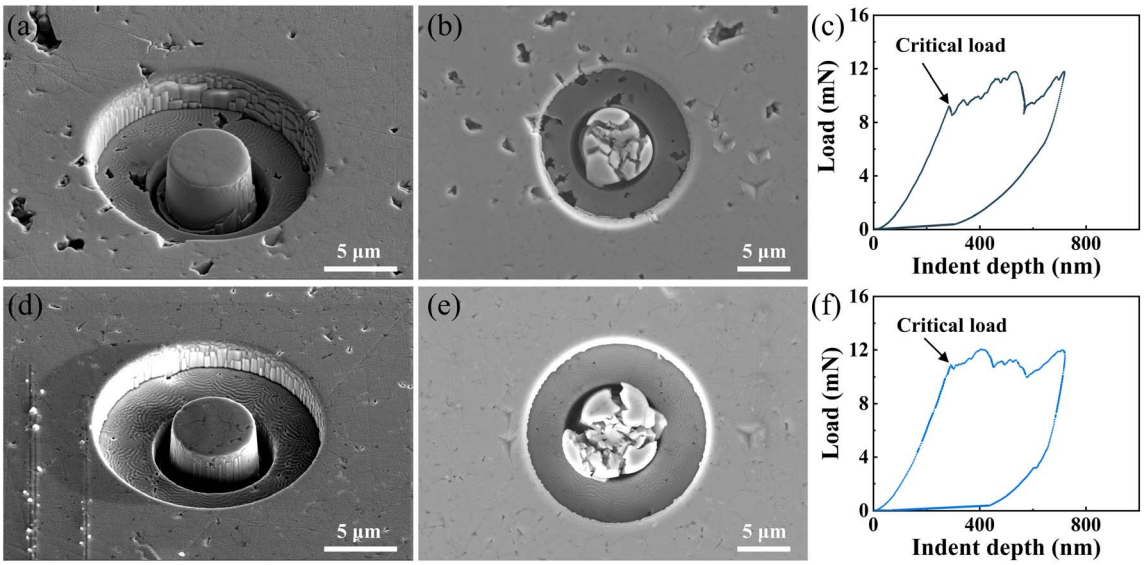

Fig. 9 (a) and (d) SEM images of micro-pillars of original NZSP and NZSP-2.5NLP produced by FIB milling; (b) and (e) top view of micro-pillars of original NZSP and NZSP-2.5NLP after indentation splitting test; (c) and (f) typical load–displacement curves of original NZSP and NZSP-2.5NLP.

mN. The calculated fracture toughness values are compiled in Table 5.

The micro-pillar splitting-based fracture toughness values are in general alignment with the VIF results. For the NZSP-2.5NLP sample, the K_{IC} obtained by micro-pillar splitting (0.68 $\pm$ 0.12 MPa $m^{0.5}$) was slightly lower than that measured by VIF (0.76 $\pm$ 0.11 MPa $m^{0.5}$). This minor discrepancy may be attributed to the complex crack propagation behavior during Vickers indentation: in addition to the primary Palmqvist cracks, secondary annular cracks form on the indentation surface. The formation of these secondary cracks consumes part of the fracture energy, thereby reducing the driving force for primary crack (Palmqvist crack) propagation and resulting in a slightly smaller measured crack length c (the sum of the crack length and the half diagonal). According to eqn (1), this reduction in c leads to a marginally overestimated K_{IC}. Unlike the VIF, micro-pillar approach overcomes the limitations in measuring cracks in porous and defect-rich samples under low loads, where empirical formulas may be inaccurate. By focusing on a small region, it also minimizes the impact of porosity on fracture toughness measurements.

4. Discussion

4.1 The effect of NLP on the microstructure of NZSP

Experimental results presented in Section 3 show that the modified NZSP samples exhibit lower porosity (Fig. 3) and a finer, more homogeneous grain-size distribution (Fig. 5) compared with the original NZSP. To clarify the underlying microstructural evolution, a schematic illustration is provided in Fig. 10.

During sintering, NLP tends to segregate to grain boundaries, particularly at grain boundary junctions (as shown in Fig. S10), in agreement with previous reports.[22,35] The accumulated NLP at these sites exerts interfacial drag on migrating grain boundaries, kinetically suppressing excessive grain growth at high temperatures. The local driving pressure for grain-boundary migration can be expressed as:

$$P = \kappa\gamma_{gb}$$

where κ is the grain-boundary curvature and γ_{gb} is the grain-boundary energy. Compared with the original NZSP, the modified NZSP samples show a considerably narrower grain-size distribution without abnormally grown grains. According to classical grain-growth theory,[36] a finer microstructure possesses a higher average curvature and would normally exhibit a larger driving force for grain-boundary migration if γ_{gb} remained unchanged. However, such accelerated coarsening is not observed experimentally. This behavior suggests that the effective driving force for grain-boundary migration is reduced in the modified samples. Such an effect may arise from NLP segregation at grain boundaries, which could decrease γ_{gb} and/or reduce grain-boundary mobility through interfacial drag.

Table 5 Experimental results of pillar splitting tests

Sample	E/H	Number of pillars	Pillar radius, R (μm)	Critical load of failure, P_c (mN)	Fracture toughness, K_{IC} (MPa $m^{0.5}$)
Original NZSP	14.1 $\pm$ 0.2	9	2.58 $\pm$ 0.08	8.6 $\pm$ 1.3	0.58 $\pm$ 0.11
NZSP-2.5NLP	13.2 $\pm$ 0.2	8	2.64 $\pm$ 0.02	10.5 $\pm$ 1.8	0.68 $\pm$ 0.12

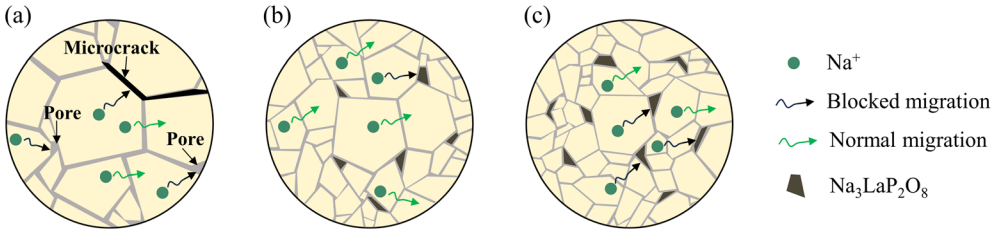

Fig. 10 Schematic diagram of the role of NLP in (a) original NZSP; (b) NZSP-2.5NLP and (c) NZSP-5NLP. NLP addition refines and homogenizes the grains while suppressing crack formation. An optimal NLP content facilitates ion migration, whereas excessive amounts may obstruct transport pathways.

Similar segregation-induced reductions in grain-boundary energy have been reported by Dey *et al.*,[37] who showed that La^{3+} segregation significantly lowered the grain-boundary energy in nanocrystalline yttria-stabilized zirconia, resulting in enhanced grain-growth resistance.

Therefore, NLP contributes through dual mechanisms: (i) kinetically, by providing interfacial drag that inhibits boundary migration; and (ii) thermodynamically, by potentially lowering the local grain-boundary energy. These combined effects enable the modified NZSP to maintain a refined and homogeneous microstructure, promoting pore elimination and leading to higher densification.

This refined microstructure also contributes to crack suppression. In NaSICON ceramics, coarse grains can accumulate significant internal stress during cooling due to anisotropic thermal contraction, leading to grain-boundary microcracks, particularly when boundaries are weak.[38] As observed in the original NZSP and NZSP-1NLP samples (Fig. 4(a and b)), larger grains and grain-size mismatch promote microcrack formation, which links intergranular voids and reduces densification (Fig. 10(a)). In contrast, the NZSP-2.5NLP and NZSP-5NLP samples exhibit refined and homogeneous grains, mitigating stress buildup and significantly suppressing grain-boundary microcracks.

4.2 The effect of NLP on the mechanical properties of NZSP

The improved microstructure induced by NLP addition results in noticeable changes in the mechanical response of NZSP. Reduced porosity increases the effective load-bearing area, contributing to a higher elastic modulus. Grain refinement and improved microstructural uniformity lower stress concentrations, enabling more efficient elastic load transfer. The enhanced hardness of the modified samples can be attributed to their higher densification and the reduced microcrack population, which together improve resistance to indentation-induced localized damage. Fracture toughness is also improved relative to the original NZSP due to the more homogeneous grain-size distribution, which provides a more uniform internal stress field and minimizes potential crack-initiation sites.

Compared with the previously reported NZSP,[19] the NZSP-2.5NLP sample shows distinct differences in mechanical properties. Its elastic modulus is 8.2% higher, likely due to its lower porosity. The hardness increases by 72.6%, reflecting the enhanced densification and reduced microcracking. In contrast, the fracture toughness value obtained in this work is lower than the previously reported value, which was determined using the VIF method. The present measurements show reductions of approximately 65% (VIF) and 69% (micropillar splitting). The close agreement between the two independent methods suggests that the discrepancy is not primarily caused by testing methodology. The NZSP reported in the literature exhibits a finer average grain size of 1.0 ± 0.3 μm in the literature, whereas the present material shows the majority of grains in the 1–3 μm range, indicating a comparatively coarser microstructure. Grain refinement is often associated with improved fracture toughness in ceramic electrolytes.[39,40] Despite the lower fracture toughness, NZSP-2.5NLP achieves a total ionic conductivity 162.9% higher than the literature value, indicating that its mechanical characteristics do not hinder ionic transport.

4.3 Microstructure-mechanics-electrical coupling

Microstructural optimization induced by NLP addition contributes to both mechanical stability and ionic transport, giving rise to a coupled microstructure–mechanics–electrical response. As discussed in Section 4.1, NLP addition reduces porosity and improves grain-boundary contact, resulting in a more continuous microstructural framework. As shown in Table 2, NZSP-2.5NLP exhibits the highest total ionic conductivity (7.1×10^{-3} S cm^{-1}). The reduced porosity and fewer intergranular defects help maintain Na^+ migration pathways (Fig. 10(b)), preventing transport interruption by gaps such as pores or microcracks. Meanwhile, the improved mechanical robustness helps suppress the formation and propagation of mechanically induced defects, further maintaining the continuity of ion-transport pathways.

However, the ionic conductivity does not vary monotonically with increasing densification. Although NZSP-5NLP shows the lowest porosity, its conductivity is lower than that of NZSP-2.5NLP. This suggests that the conductivity enhancement cannot be attributed solely to densification and may also be related to the spatial distribution of NLP at grain boundaries and grain boundary junctions. In the original NZSP, grain-size mismatch and thermal stress during cooling tend to generate microcracks and voids at grain boundary junctions, which originate from local mechanical stress concentration and can act as transport-limiting regions by interrupting Na^+ migration

pathways. A moderate amount of NLP helps suppress such defects, improves grain-boundary contact, and enhances the mechanical integrity of the microstructure, resisting crack formation during cooling and preserving continuous ion-transport pathways. Excessive NLP may introduce local transport hindrance due to its insulating nature (σ_{total} in the range of $\sim10^{-12}$ S cm^{-1} at RT, reported in ref. 22) and the increased grain-boundary fraction caused by further grain refinement, partially offsetting the benefit of densification (Fig. 10(c)).

Overall, these results highlight the importance of optimizing the NLP content, providing useful guidance for the compositional design and processing of NaSICON-type solid electrolytes for improved mechanical stability and ionic transport.

5. Conclusion

This study systematically investigated the effect of $Na_3LaP_2O_8$ (NLP) incorporation on the microstructure, mechanical properties, and ionic conductivity of $Na_{3.4}Zr_2Si_{2.4}P_{0.6}O_{12}$ (NZSP) solid electrolytes. The results demonstrate that controlled NLP addition effectively tailors the grain boundary structure and mechanical integrity of NaSICON ceramics. Specifically, NLP promotes grain refinement, enhances grain size uniformity, suppresses microcrack formation, reduces porosity, and improves overall densification. As a result, the elastic modulus increased by 15.6% (from 69.4 $\pm$ 7.2 GPa to 80.2 $\pm$ 1.2 GPa), hardness by 61.2% (from 4.9 $\pm$ 1.2 GPa to 8.11 $\pm$ 0.96 GPa), and fracture toughness by 17.2% (from 0.58 $\pm$ 0.11 MPa m$^{0.5}$ to 0.68 $\pm$ 0.12 MPa m$^{0.5}$). These results, verified by both Vickers indentation and micro-pillar splitting methods, confirm that NLP enhances the mechanical resilience of NZSP through densification and grain boundary strengthening.

At moderate NLP contents (up to 2.5 mol%), the increase in overall ionic conductivity indicates that mechanical reinforcement and efficient ion transport can coexist. However, higher NLP concentrations (5 mol%) reduce conductivity due to the insulating nature of NLP and excessive grain boundary fraction, revealing a compositional trade-off between mechanical and electrical performance.

Author contributions

Xingyu Liu: writing – original draft, data curation, investigation, formal analysis, visualization. Jürgen Peter Gross: writing – review and editing, methodology, visualization. Qianli Ma: conceptualization, data curation, investigation. Frank Tietz: writing – review and editing. Jürgen Malzbender: conceptualization, methodology, project administration, supervision, writing – review and editing. Ruth Schwaiger: supervision, resources, writing – review and editing.

Conflicts of interest

The authors declare no conflicts of interest.

Data availability

The data obtained in this study can be obtained from the corresponding author upon reasonable request.

Supplementary information (SI) is available. See DOI: https://doi.org/10.1039/d6ta01036a.

Acknowledgements

The authors thank Dr D. Grüner and Mr M. Ziegner for their assistance with SEM, EDX and XRD investigations. Xingyu Liu gratefully acknowledges the China Scholarship Council Funding (No. 202308120016) for financial support.

References

1 Y. Li, M. Li, Z. Sun, Q. Ni, H. Jin and Y. Zhao, *Energy Storage Mater.*, 2023, **56**, 582–599.
2 J. Janek and W. G. Zeier, *Nat. Energy*, 2016, **1**, 1–4.
3 C. Zhao, L. Liu, X. Qi, Y. Lu, F. Wu, J. Zhao, Y. Yu, Y. S. Hu and L. Chen, *Adv. Energy Mater.*, 2018, **8**, 1703012.
4 A. Chakraborty, R. Thirupathi, S. Bhattacharyya, K. Singh and S. Omar, *J. Power Sources*, 2023, **572**, 233092.
5 P. Jiang, G. Du, Y. Shi, F. She, P. Guo, G. Qian, X. Lu, F. Xie and X. Lu, *Chem. Eng. J.*, 2023, **451**, 138771.
6 Z. Gao, J. Yang, H. Yuan, H. Fu, Y. Li, Y. Li, T. Ferber, C. Guhl, H. Sun, W. Jaegermann, R. Hausbrand and Y. Huang, *Chem. Mater.*, 2020, **32**, 3970–3979.
7 Q. Ma, C. L. Tsai, X. K. Wei, M. Heggen, F. Tietz and J. T. S. Irvine, *J. Mater. Chem. A*, 2019, **7**, 7766–7776.
8 V. Jabbari, V. Yurkiv, M. G. Rasul, A. H. Phakatkar, F. Mashayek and R. Shahbazian-Yassar, *Energy Storage Mater.*, 2023, **57**, 1–13.
9 J. S. Kim, G. Yoon, S. Kim, S. Sugata, N. Yashiro, S. Suzuki, M. J. Lee, R. Kim, M. Badding, Z. Song, J. Chang and D. Im, *Nat. Commun.*, 2023, **14**, 782.
10 F. Li, K. Ren, M. Hou, M. Lin, X. Yang, Y. Zhou, S. Xiong and F. Liang, *ACS Energy Lett.*, 2025, **10**, 195–204.
11 K. Ren, H. Zhou, D. Zhang, D. Yang, F. Li, X. Zhang, P. Liu, Y. Zhou, P. Dong, X. Feng, H. Wu, K. Hayashi, B. Yang and F. Liang, *Adv. Energy Mater.*, 2025, **15**, e00472.
12 Z. Deng, Z. Wang, I. H. Chu, J. Luo and S. P. Ong, *J. Electrochem. Soc.*, 2015, **163**, A67.
13 C. Monroe and J. Newman, *J. Electrochem. Soc.*, 2005, **152**, A396.
14 F. P. McGrogan, T. Swamy, S. R. Bishop, E. Eggleton, L. Porz, X. Chen, Y. M. Chiang and K. J. Van Vliet, *Adv. Energy Mater.*, 2017, **7**, 1602011.
15 W. Manalastas Jr, J. Rikarte, R. J. Chater, R. Brugge, A. Aguadero, L. Buannic, A. Llordés, F. Aguesse and J. Kilner, *J. Power Sources*, 2019, **412**, 287–293.
16 G. Bucci, T. Swamy, Y. M. Chiang and W. C. Carter, *J. Mater. Chem. A*, 2017, **5**, 19422–19430.
17 J. Wolfenstine, W. Go, Y. Kim and J. Sakamoto, *Ionics*, 2023, **29**, 1–8.
18 J. F. Nonemacher, S. Naqash, F. Tietz and J. Malzbender, *Ceram. Int.*, 2019, **45**, 21308–21314.

19 J. P. Gross, G. Dück, F. Schäfer, M. Holzapfel, M. Finsterbusch, J. Malzbender and R. Schwaiger, *J. Mater. Sci.*, 2023, **58**, 144–156.
20 B. Hitesh and A. Sil, *J. Am. Ceram. Soc.*, 2023, **106**, 6743–6754.
21 W. Xie, Z. Deng, Z. Liu, T. Famprikis, K. T. Butler and P. Canepa, *Adv. Energy Mater.*, 2024, **14**, 2304230.
22 Z. Zhang, Q. Zhang, J. Shi, Y. Chu, X. Yu, K. Xu, M. Ge, H. Yan, W. Li, L. Gu, Y. Hu, H. Li, X. Yang, L. Chen and X. Huang, *Adv. Energy Mater.*, 2017, **7**, 1601196.
23 L. Liu, Q. Ma, X. Zhou, Z. Ding, D. Grüner, C. Kübel and F. Tietz, *J. Power Sources*, 2025, **626**, 235773.
24 Q. Ma, M. Guin, S. Naqash, C. L. Tsai, F. Tietz and O. Guillon, *Chem. Mater.*, 2016, **28**, 4821–4828.
25 C. A. Schneider, W. S. Rasband and K. W. Eliceiri, *Nat. Methods*, 2012, **9**, 671–675.
26 International Organization for Standardization, *ISO 14577-1:2015, Metallic Materials - Instrumented Indentation Test for Hardness and Materials Parameters-Part 1: Test Method*, Geneva, 2015.
27 C. B. Ponton and R. D. Rawlings, *Mater. Sci. Technol.*, 1989, **5**, 865–872.
28 C. B. Ponton and R. D. Rawlings, *Mater. Sci. Technol.*, 1989, **5**, 961–976.
29 B. R. Lawn and E. R. Fuller, *J. Mater. Sci.*, 1975, **10**, 2016–2024.
30 M. Sebastiani, K. Johanns, E. G. Herbert, F. Carassiti and G. M. Pharr, *Philos. Mag.*, 2015, **95**, 1928–1944.
31 J. G. L. Alexander, M. Gaurav, K. N. Tee, M. Johann and M. K. Alexander, *Proc. SPIE 9668, Micro+Nano Materials, Devices, and Systems*, New South Wales, Sydney, 2015, vol. 9668, p. 96685S.
32 M. Sebastiani, K. Johanns, E. G. Herbert and G. M. Pharr, *Curr. Opin. Solid State Mater. Sci.*, 2015, **19**, 324–333.
33 S. Naqash, Q. Ma, F. Tietz and O. Guillon, *Solid State Ionics*, 2017, **302**, 83–91.
34 X. S. Zhao, S. L. Shang, Z. K. Liu and J. Y. Shen, *J. Nucl. Mater.*, 2011, **415**, 13–17.
35 W. Li, N. Zhao, Z. Bi and X. Guo, *Appl. Phys. Lett.*, 2022, **121**, 033901.
36 M. Hillert, *Acta Metall.*, 1965, **13**, 227–238.
37 S. Dey, C.-H. Chang, M. Gong, F. Liu and R. H. R. Castro, *J. Mater. Res.*, 2015, **30**, 2991–3002.
38 S. D. Jackman and R. A. Cutler, *J. Power Sources*, 2012, **218**, 65–72.
39 J. F. Nonemacher, Y. Arinicheva, G. Yan, M. Finsterbusch, M. Krüger and J. Malzbender, *J. Eur. Ceram. Soc.*, 2020, **40**, 3057–3064.
40 M. Wang, X. F. Wang, W. C. Bao, Y. Chen, T. He, S. Z. Lv, D. Y. Jiang and X. G. Wang, *J. Am. Ceram. Soc.*, 2026, **109**, e70412.